



Carbon-quantum-dots-involved Fe/Co/Ni phosphide open nanotubes for high effective seawater electrocatalytic decomposition

Shujuan Lv^a, Ying Deng^{a,c}, Qian Liu^a, Ziqi Fu^a, Xiaobin Liu^c, Minghui Wang^a, Zhenyu Xiao^{a,*}, Bin Li^{a,b,**}, Lei Wang^{a,c,**}

^a State Key Laboratory Base of Eco-Chemical Engineering, International Science and Technology Cooperation Base of Eco-chemical Engineering and Green Manufacturing, College of Chemistry and Molecular Engineering, Qingdao University of Science and Technology, Qingdao 266042, PR China

^b College of Materials Science and Engineering, Qingdao University of Science and Technology, Qingdao, Shandong 266042, China

^c College of Environment and Safety Engineering, Qingdao University of Science and Technology, Qingdao 266042, China

ARTICLE INFO

Keywords:

Metal-organic frameworks
Open hollow structure
Etching
Trimetallic phosphide
Seawater splitting

ABSTRACT

The hollow materials with open structure can accelerate the mass transfer and bubble release rate, which have attracted tremendous attention for electrocatalytic water splitting. In this work, a unique tri-metal phosphide open nanotube structure [FeCoNiP@carbon quantum dots, FCNP@CQDs] is firstly fabricated by a selected etching and phosphating process with a MIL-88A@CQDs (MIL stands for Material of Institute Lavoisier) as the precursor. Benefiting from their open structure, FCNP@CQDs exhibit excellent catalytic performance. In alkaline seawater solution, a low overpotential of 268 mV is required to reach 20 mA cm⁻² current density for oxygen evolution reaction, while the η_{20} of hydrogen evolution reaction is 150 mV. The FCNP@CQDs//FCNP@CQDs electrolyzer requires a voltage of 1.61 V to reach 10 mA cm⁻². The integrated strategy of CQDs-doping and construction of hollow open structures may open a new and relatively unexplored path for fabricating high-performance seawater splitting catalysis.

1. Introduction

Hydrogen (H₂), a perfect clean energy candidate, has been recognized as the future energy to solve the ever-increasing energy demand and environmental pollution due to its high energy density (120 MJ kg⁻¹, three times higher than gasoline) [1], excellent combustion property [2], rich element content and zero-carbon emission [3,4]. Electrochemical water splitting technology is among the most efficient path for hydrogen production [5–7], which not only directly produces H₂ and O₂ with high purity, but also effectively uses the excess green electricity generated by sustainable energy resources (solar, wind, tidal, geothermal) [8–10]. However, the hydrogen market is dominated by fossil fuel reduction strategies, nowadays. The H₂ produced by electrochemical hydrogen evolution reaction (HER) captures less than 5% market share due to the expensive noble metal catalyst and the scarcity of pure water [11–14]. In this content, H₂ production from wastewater or seawater system with non-noble metal catalysts presents higher practical application value and has drawn increasing attention of the

scientific community [15–18]. In a seawater system, the competitive chlorine evolution reaction (CER) with the potential 480 mV higher than the oxygen evolution reaction (OER, 1.23 V vs. RHE) in an alkaline environment can produce hypochlorite, which leads to the corrosion of anodic materials for low stability performance [19–22]. Hence, the rational construction of HER and OER catalysts with lower reaction overpotential are imperative, yet challenge, to suppress the CER for excellent energy conversion efficiency and lifespan.

Transition metal phosphides (TMPs) are already widely used for catalytic water splitting owing to their metal-like conductivity and high intrinsic activity toward both HER and OER processes [23–27]. To promote the mass transfer and adsorption/desorption of intermediates and products, one strategy is to design TMPs with various morphology to provide more surface area and rich channels for fast gas escaping from the electrode surface [28–33]. Among these, hollow structure, especially open hollow structure, with well-defined open shell and interior voids can promote the transfer ratio of reactant and gas for outstanding water splitting activity [34–36]. Chen and co-workers fabricate hollow CoP

* Corresponding author.

** Corresponding authors at: State Key Laboratory Base of Eco-Chemical Engineering, International Science and Technology Cooperation Base of Eco-chemical Engineering and Green Manufacturing, College of Chemistry and Molecular Engineering, Qingdao University of Science and Technology, Qingdao 266042, China.

E-mail addresses: inorgxiaozenyu@163.com (Z. Xiao), binli@qust.edu.cn (B. Li), inorchemwl@126.com (L. Wang).

<https://doi.org/10.1016/j.apcatb.2023.122403>

Received 26 July 2022; Received in revised form 1 November 2022; Accepted 16 January 2023

Available online 18 January 2023

0926-3373/© 2023 Elsevier B.V. All rights reserved.

nano-frame with open structure, exhibiting great HER and OER catalytic activity than common hollow CoP nano-materials due to their unique open frame [37]. The other strategy is to adjust the electronic structure of TMPs for enhanced intrinsic activity by element doping [38,39], defect engineering [40], interface and crystal-face regulation et al. [41–43]. For example, Yamauchi et al. report the synergistic effect of metal elements in hollow NiCoFeP nanocubes. A low OER and HER overpotential at 10 mA cm⁻² of 273 mV and 131 mV is achieved in alkaline electrolyte [29]. Ren et al. demonstrate a carbon quantum dots (CQDs)-doped Mn_xNi_{5-x}P₄ nanosheet with a lower HER overpotential of 56 mV than that of Mn_xNi_{5-x}P₄ nanosheet (η_{10} = 99 mV). Notably, the abundant -COOH and -OH functional groups of CQDs can strongly couple with TMPs to provide more lattice defect and rich heterogeneous interface as well as improved conductivity [44]. Therefore, the talented integration of open hollow structure, optimized intrinsic activity and functionalized CQDs into TMPs is promising to provide a possible way for high-performance seawater splitting catalyst.

Herein, we firstly report CQDs doped tri-metal FeCoNiP open nanotube (FCNP@CQDs) via sequenced etching and phosphatizing MIL-88A@CQDs (MIL stands for Material of Institute Lavoisier) precursor as bifunctional catalyst (HER and OER) for the seawater splitting. The CQDs doped MIL-88A nanorods are prepared by reflux process, followed by simple selective etching under hydrothermal conditions to obtain hollow FCN-LDHs@CQDs nanotubes with an open structure. After a gaseous phosphating process, the target amorphous FCNP@CQDs nanotube is obtained, which provides high surface area, fast gas, and reactant transfer rate and enhanced intrinsic activity for HER and OER process. The optimized FCNP@CQDs nanotube presents a low OER and HER overpotential of 268 and 150 mV to reach 20 mA cm⁻² current density in the alkaline seawater, respectively. Furthermore, an alkaline seawater electrolyzer is fabricated with FCNP@CQDs as both the cathode and anode. A potential of 1.61 V is required at 10 mA cm⁻², which is even better than the commercial 20% Pt/C and RuO₂ electrocatalysts (1.73 V). The selective etching and CQDs-involved strategy provide an avenue for the construction of functional open hollow structure electrode materials for energy storage and conversion application.

2. Experimental section

2.1. Chemicals

Fe(NO₃)₃·9H₂O (99.0%), Co(NO₃)₂·6H₂O (99.0%) and KOH (85.0%) are purchased from Aladdin Reagent Inc. Corporation (China). Ni(NO₃)₂·6H₂O is provided by Tianjin Dingshengxin Chemical Industry Co., Ltd. Fumaric acid (C₄H₄O₄, ≥98.0%) is provided by Energy Chemical Co., Ltd. NaOH (≥96.0%), urea (≥99.0%) and ethanol (≥99.7%) are provided by Sinopharm Chemical Reagent Co., Ltd. Sodium hypophosphite (NaH₂PO₂, 98–101%) is provided by Shanghai McLean Biochemical Technology Co., Ltd. Perfluorosulfonic acid-PTFE copolymer (Nafion; 5% w/w in water, Sigma-Aldrich). All chemicals are used directly after purchase.

2.2. Materials synthesis

2.2.1. Synthesis of carbon quantum dots (CQDs)

Using two platinum plates (1*1 cm) as anode and counter electrode, a dark brown solution is obtained by an electrolytic process of 20 Voltage for 24 h with a 150 mL mixed solution of ethanol and distilled water (v:v = 14:1) containing 1.0 g of NaOH as electrolyte. Then, take the supernatant by centrifuge, and deposited NaOH salt out by adding 150 mL of ethanol to the resulting supernatant. After evaporating the supernatant, a red-brown seriflux is obtained and further dispersed in 100 mL of deionized water. The as-prepared suspension is dialyzed for 24 h for 5–7 times to remove residual NaOH and the neutral CQDs solution with the concentration of 4 mg/mL is obtained.

2.2.2. Synthesis of MIL-88A@CQDs nanorods

Fumaric acid (140 mg) is dissolved in 20 mL water in an oil bath at 70 °C to obtain solution A, and Fe(NO₃)₃·9H₂O (530 mg) is dissolved in 5 mL water at room temperature to obtain solution B. Then solution B and CQDs solution (2 mL) are poured into solution A and stirred in an oil bath at 110 °C for 6 h. After cooling to RT (room temperature), the resulting precipitate (MIL-88A@CQDs) is collected by centrifuged and washed with ethanol, and dried at 60 °C. As a contrast, the samples with different CQDs are prepared by adding 0 mL, 1 mL, or 3 mL CQDs solution, and named as MIL-88A, MIL-88A@CQDs-1, and MIL-88A@CQDs-3, respectively.

2.2.3. Synthesis of FCN-LDHs@CQDs nanotubes

MIL-88A@CQDs (38.5 mg) is dispersed in 14 mL ethanol (solution A); Co(NO₃)₂·6H₂O (393.75 mg), Ni(NO₃)₂·6H₂O (131.25 mg), and urea (350 mg) are dissolved in 21 mL water (Solution B). The two solutions are mixed, and then poured into Teflon-lined reactors. After heating at 90 °C for 5 h, the FCN-LDHs@CQDs nanotubes are prepared by washing and drying at 60 °C.

As a contrast, the LDH samples with different CQDs are synthesized by employing MIL-88A, MIL-88A@CQDs-1, and MIL-88A@CQDs-3 as precursors, and named as FCN-LDHs, FCN-LDHs@CQDs-1, and FCN-LDHs@CQDs-3, respectively. Meanwhile, the Co:Ni ratio is also optimized by adjusting the ratio of cobalt nitrate and nickel nitrate (total 525 mg, x:y = 1:0, 1:1, 2:1, 3:1, 4:1 or 0:1), and the related products are named as FCN-LDHs@CQDs-x:y, respectively.

2.2.4. Synthesis of FCNP@CQDs nanotubes

FCNP@CQDs nanotubes are synthesized by a typical low-temperature phosphating method. FCN-LDHs@CQDs nanotubes (17.4 mg) and NaH₂PO₂ (212 mg) are placed in two different positions of a porcelain boat. After heating at 300 °C for 2 h in a tube furnace at a heating rate of 2 °C·min⁻¹ under the condition of nitrogen flow, the target product FCNP@CQDs nanotubes are prepared. As a contrast, a series of products are synthesized by changing the precursors to MIL-88A, the phosphating temperature, and the phosphating dose, and named as FCNP, FCNP@CQDs-X (X = 250 °C, 350 °C), FCNP@CQDs-D (2 times the amount of phosphating), and FCNP@CQDs-F (4 times the amount of phosphating), respectively.

2.3. Characterization of samples

The crystalline phase is confirmed by powder X-ray diffraction (PXRD, PROX-ray diffractometer with Cu K α source) with a scan range of 5–90°. The morphology and structure are characterized by scanning electron microscopy (SEM, Hitachi, S-4800) and transmission electron microscope (TEM, JEM-2100UHR, 200 KV working voltage). The chemical compositions are confirmed by X-ray photoelectron spectroscopy (XPS, Thermo Fisher Scientific, Escalab 250Xi). The specific surface area of the samples is characterized by N₂ adsorption-desorption isotherms at 77 K (micromeritics instruments version 5.03). *In-situ* Raman spectra were obtained under operating conditions using a specially designed electrolytic cell consisting of a working electrode at the bottom, a platinum wire (counter electrode), and an Ag/AgCl electrode (reference electrode). The laser wavelength of the experiments is 532 nm, and the microscope is a confocal Raman microscope (inVia Qontor, Renishaw) with a 60X objective.

2.4. Electrochemical measurements

The electrocatalytic activities of the catalysts for OER and HER are tested under the three-electrode structure, with Ag/AgCl (saturated KCl) and graphite rod as reference electrode and counter electrode, respectively. The test process is performed with Gamry Reference 3000 workstation under 1 M KOH seawater solution as electrolyte. The catalyst suspension contains 2.5 mg of catalyst powder, 0.45 mL of

ethanol and 50 μL of Nafion solution. The working electrode is prepared on carbon paper supports ($0.5 \times 0.3 \text{ cm}$) with the catalyst suspension. The polarization curves for OER and HER are carried out with the same scan rate of 5 mV s^{-1} . The Electrochemical Impedance Spectroscopy (EIS) measurements are from 100KHz to 0.1 Hz. The potentials in this experiment refer to the reversible hydrogen potential (RHE), $E_{\text{RHE}} = E_{\text{Ag/AgCl}} + 0.0592 \text{ pH} + 0.1989$. The overpotential is calculated according to the following formula: $\eta = E_{\text{RHE}} - 1.23 \text{ V}$. H_2 evolution rate $v = \text{H}_2(\text{volume})/(22.4 \text{ *t})$.

3. Results and discussion

3.1. Synthesis and structural characterization of catalysts

The synthetic process of CQDs embedded trimetallic (Fe, Co, and Ni) phosphide nanotubes (FCNP@CQDs) is demonstrated in Fig. 1. At the first step, the CQDs-doped MIL-88A (MIL-88A@CQDs) is successfully prepared by adding CQDs suspension to the synthesis of MIL-88A. Secondly, the CQDs-doped FCN-LDHs are prepared by a selective chemical etching and interface-regulated LDH regrowth processes with MIL-88A@CQDs as a template. The NH_3 molecules originated from the decomposition of urea etch the framework of MIL-88A to release complex Fe-NH_3 ions (Equations S1 and S2). Afterward, the released Fe-NH_3 ions co-precipitate with Co^{2+} , Ni^{2+} , and OH^- to form a hydroxide shell (FCN-LDHs) (Equations S3 and S4) [45]. With the continuous etching process, the free ions accumulate at the FCN-LDHs interface and gradually self-assemble to form the FCN-LDHs@CQDs. Finally, through a gaseous phosphating process of NaH_2PO_2 under N_2 atmosphere, the FCN-LDHs@CQDs nanotube is transferred to FCNP@CQDs nanotubes with maintained morphology.

The scanning electron microscopy image (SEM) shows that the MIL-88A displays a nanorod morphology with a diameter of $0.5 \times 0.5 \times 4 \mu\text{m}$ (Fig. S1). After the CQDs doping process, the SEM image (Fig. 2a) displays that the MIL-88A@CQDs presents similar morphology with MIL-88A. However, the crystallinity of MIL-88A@CQDs is obviously decreased (Fig. S2) due to the defects produced during CQDs involved process. This kind of defect is beneficial for the further etching process. After the selective etching process driven by urea, the MIL-88A framework is gradually dissolved and the released Fe^{3+} ions co-precipitate with Co^{2+} , Ni^{2+} and OH^- ions along the side-face to form the hollow FCN-LDHs@CQDs nanotubes (Fig. 2b). According to the diameter size and wall thickness size distribution images (Fig. S3), the diameter size of nanotubes is focused on the range of 575–625 nm and the wall thickness in the range of 43–53 nm. The transmission electron microscopy (TEM) images also further demonstrate the hollow structure of FCN-LDHs@CQDs nanotubes and the existence of Fe, Co, Ni, and O elements in the corresponding mapping images (Fig. S4). As shown in the powder X-ray diffraction (PXRD) pattern, the characteristic peaks of the MIL-88A@CQDs precursor are completely disappeared, indicating the framework of MIL-88A is destroyed (Fig. S5). Without the urea, the nanorod structure of MIL-88A@CQDs is well maintained. However, the corresponded surface is covered by irregular Co/Ni-based

nanoparticles (Fig. S6), which indicates the important effect of urea during the etching process. The obvious mass loss of 22.7% during 220–360 $^\circ\text{C}$ in the TGA (Thermogravimetric Analysis, Fig. S7) process corresponding well with the reported dehydration reaction of the OH^- group in hydroxide. The corresponded molecule formula can be defined as $\text{M}(\text{OH})_{2.7-0.75} \text{H}_2\text{O}$ ($\text{M} = \text{Fe/Co/Ni}$). The Energy dispersive X-ray (EDX) spectroscopic images show that Fe, Co, Ni, C, and O are distributed uniformly in FCN-LDHs@CQDs nanotubes (Fig. S8) and the element ratio of Fe:Co:Ni is 9:3:1. After gaseous phosphating process, the FCNP@CQDs maintains well nanotube structure of FCN-LDHs@CQDs. However, some nanoparticles are produced on the surface of nanotube and the thickness of tube wall is decreased to about $\sim 35 \text{ nm}$ (Fig. 2c). As shown in Fig. 2d, TEM image further confirms its hierarchical hollow nanotube structure constructed by nanoparticles. High-resolution TEM (HRTEM) image (Fig. 2e) shows clear lattice spacing of 0.267 nm corresponding to the (020) plane of carbon quantum dots, and the indistinct lattice in the marked region of Fig. 2e corresponds to low crystalline or amorphous phase Fe/Co/Ni phosphide. The presence of Fe, Co, Ni, and P elements in the mapping spectrum proves that the phosphating is successful (Fig. 2f-k).

Furthermore, the effect of Co-Ni ratio and CQDs content on the reaction process and product morphology are also explored. For the samples obtained without $\text{Co}(\text{NO}_3)_2 \cdot 6\text{H}_2\text{O}$, a hollow nanorod structure with closed ends is obtained, which presents obvious hierarchical morphology constructed by a series of curving FN-LDHs@CQDs nanoflakes (Fig. 3a). The PXRD pattern of FN-LDHs@CQDs displays mixed diffraction peaks of $\text{Ni}(\text{OH})_{2-0.75} \text{H}_2\text{O}$ and MIL-88A (Fig. 4a), indicating that the formation of layered double hydroxides (LDH) phase and the MIL-88A framework is not completely etched due to slow diffusion ratio of etching reagent caused by hollow nanorod structure with closed ends. With the increase of Co element, the surface nanoflakes are gradually disappeared and the closed ends are opened. For the FCN-LDHs@CQDs-2:1 sample (Fig. 3c), it is observed that the surface FCN-LDHs@CQDs nanoflakes present obvious broken edge and a part of ends of nanorods are opened to form nanotube structure. When the Co:Ni ratio is up to 3:1, the open hollow FCN-LDHs@CQDs nanotubes are completely formed (Fig. 3d) and the nanoflakes also completely disappeared corresponding to an amorphous phase (Fig. 4a). With the further increasing of Co:Ni ratio, some cracks and breakages are appeared at the outer shell of the nanotubes (Fig. 3e). For the sample with Co:Ni ratio of 1:0 (Fig. 3f), the significant collapses of the nanotube can be observed due to too much cracks existence. When no metal is added during the etching process, LDH could not be formed due to the lack of metal elements combined with OH^- . As a result, the MIL-88A@CQDs are etched and collapsed (Fig. S9). The CQD content also presents an obvious effect on the morphology and structure of products. For the etching process of MIL-88A without CQDs, the open hollow nanotubes cannot be formed (Fig. S10a). When the amount of CQDs is increased, the target open nanotubes with open ends can be formed (Figs. S10b and S10c). However, the further increasing of CQDs amount causes complete collapse of the nanotube structure (Fig. S10d), due to the rigidity of FCN-LDHs is decreased by increased of CQDs content. Therefore, both the Co-Ni ratio

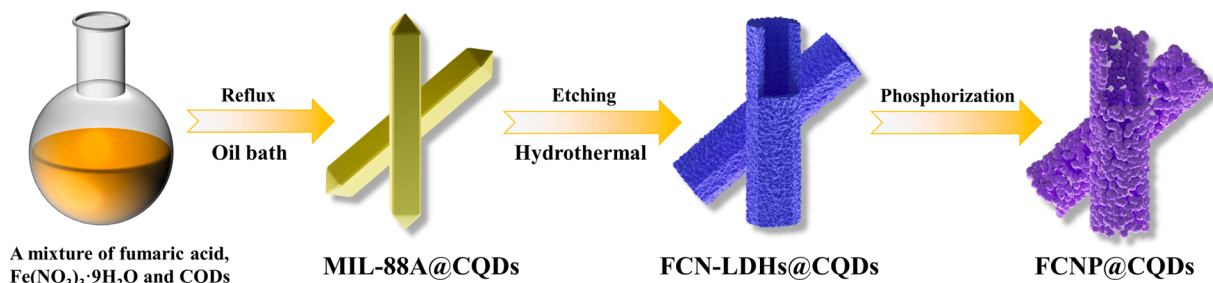


Fig. 1. Schematic of the synthesis process of open hollow FCNP@CQDs nanotube via MIL-88A@CQDs as a template. The NH_3 (from urea hydrolysis) driving etching and Ostwald ripening prepared the FCN-LDHs@CQDs, which is further phosphating to form target FCNP@CQDs.

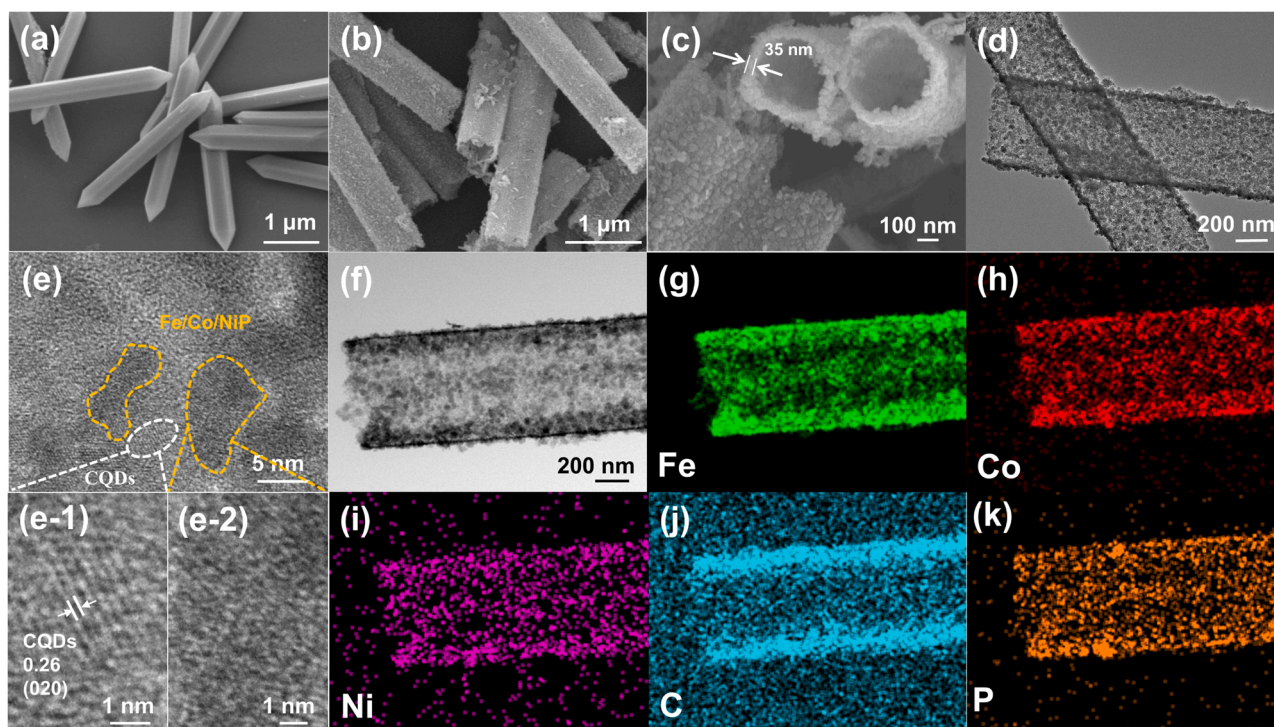


Fig. 2. SEM images: (a) MIL-88A@CQDs; (b) FCN-LDHs@CQDs; and (c) FCNP@CQDs. (d) TEM image; (e) HRTEM images; and (f) TEM image of a FCNP@CQDs nanotube and the corresponding mapping for (g) Fe, (h) Co, (i) Ni, (j) C and (k) P.

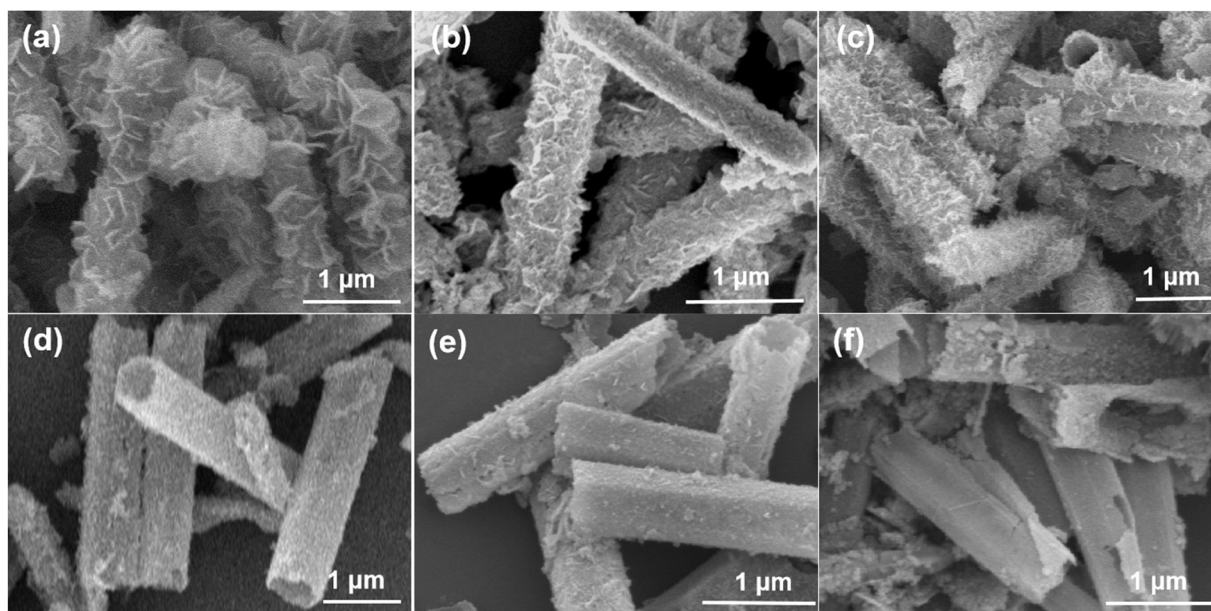


Fig. 3. SEM images: (a) FN-LDHs@CQDs; (b) FCN-LDHs@CQDs-1:1; (c) FCN-LDHs@CQDs-2:1; and (d) FCN-LDHs@CQDs; (e) FCN-LDHs@CQDs-4:1; (f) FC-LDHs@CQDs.

and CQDs content can adjust the etching process and the morphology product. The Ni element can enhance the stability FCN-LDHs while the Co element and CQDs can decrease the rigidity of FCN-LDHs. Consequently, the suitable stability and rigidity of FCN-LDHs can form the target hollow nanotube structure which is beneficial for the fast mass transfer with enhanced electrochemical performance.

There are no obvious diffraction peaks in PXRD patterns (Fig. 4a), indicating a low crystalline phase or amorphous phase of FCNP@CQDs. Compared with the reported products, the low crystalline phase may

attribute to the co-doping of tri-metal elements (Fe, Co, and Ni) and the involved CQDs, which produce lots of defects and lattice distortion [46]. The electron paramagnetic resonance (EPR) results (Fig. 4b) confirm the existence of P vacancy defect with obvious signal at $g = 2.003$ of both FCNP@CQDs and FCNP [47,48]. The stronger signal of FCNP@CQDs demonstrates that the involved CQDs are beneficial to the formation of the defect in FCNP. Nitrogen adsorption/desorption tests are performed, and the obtained isotherms and pore size distributions are shown in Fig. 4c. The curve shapes of FCNP@CQDs and FCNP can be assigned to

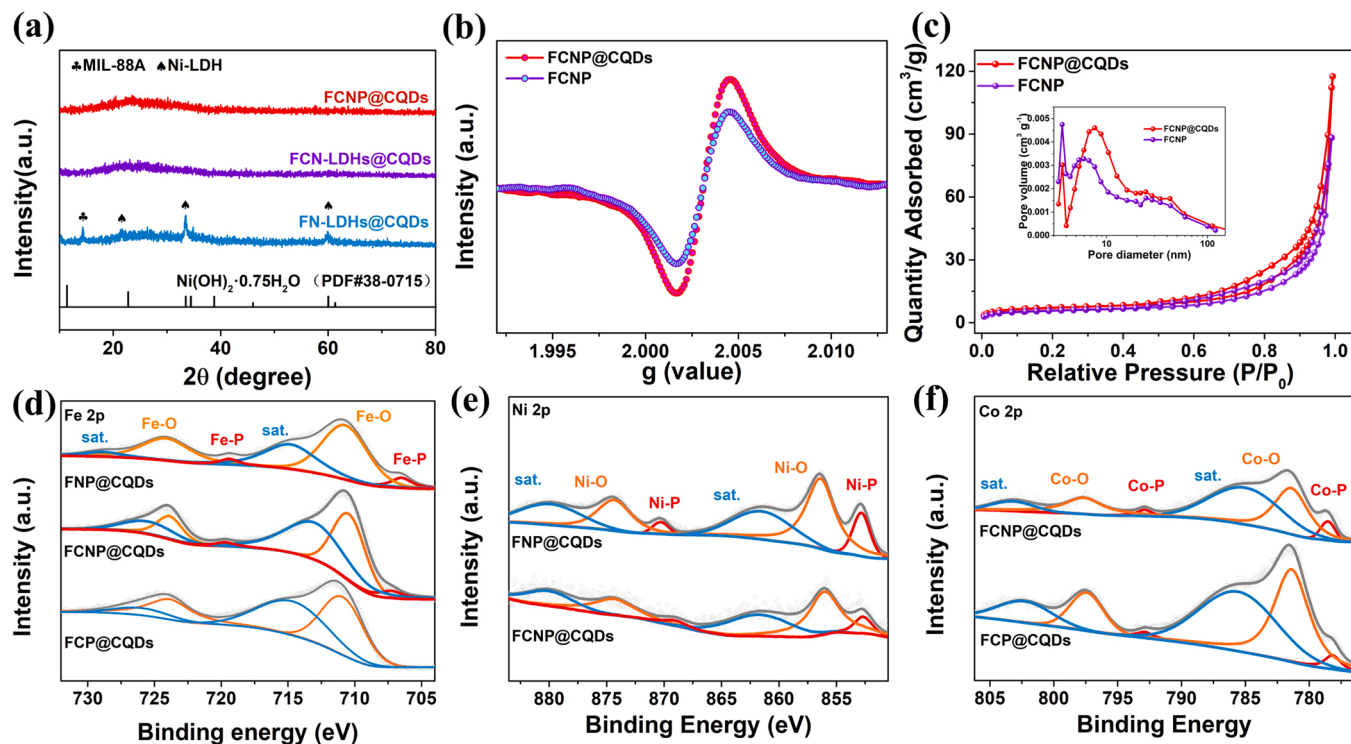


Fig. 4. (a) PXRD patterns of FN-LDHs@CQDs, FCN-LDHs@CQDs, and FCNP@CQDs; (b) EPR spectra of FCNP and FCNP@CQDs; (c) N₂ adsorption-desorption isotherms of FCNP@CQDs and FCNP; (d) Fe 2p, (e) Ni 2p, and (f) Co 2p orbital XPS spectra of FNP@CQDs, FCNP@CQDs and FCP@CQDs.

type IV isotherms (representing mesoporous materials) and the specific surface area of FCNP@CQDs is calculated to be 310 m²/g, as well as being higher than the 250 m²/g of FCNP. The BJH (Barret-Joyner-Halenda) pore size distribution of FCNP@CQDs presents a wide mesoporous range, and the pore width of FCNP@CQDs and FCNP are 7.6 and 5.9 nm, respectively, which is benefit for the rapid diffusion of electrolyte and the overflow of bubbles. To explore the surface electronic interactions of different elements, the X-ray Photoelectron Spectroscopy (XPS) of FCNP@CQDs, FCP@CQDs, and FNP@CQDs is performed. As shown in Fig. S11, the result further confirms that the Fe, Co, and Ni elements are involved in the tube shell of FCNP@CQDs during the etching process. The high-resolution Fe spectrum of FCNP@CQDs displays the existence of Fe-P species with a pair of fitted peaks at 707.2 and 719.6 eV and Fe-O species at 710.6 and 723.9 eV (Fig. 4d). For the FNP@CQDs sample without Co element, the fitted peaks of Fe-P species present lower bonding energy with the value of 706.3 and 719.4 eV, which demonstrates that the doped Co elements can adjust the electron structure of Fe center. A similar phenomenon can also be observed in Fig. 4e, the peaks in Ni-P species at 852.6 and 869.0 eV of FCNP@CQDs are shifted to 852.8 and 870.3 eV for the FNP@CQDs sample. Meanwhile, it is also observed that the involved Ni element can affect the binding energy of the Co element. The binding energy of Co-P peaks of FCNP@CQDs at 778.5 and 792.9 eV are decreased to 778.4 and 792.8 eV (Fig. 4f). Furthermore, the Fe, Co, and Ni elements of the three samples all present obvious peaks of high valence M³⁺ or M²⁺ according to the surface oxidation [49], and the ratio of M^{3+/2+} peak area and M⁰ peak area is gradually increased with the increasing of Co element, which may be attributed to the gradually opened and collapsed nanotube structure (Fig. 3f).

3.2. Electrochemical analysis for OER, HER, and overall seawater splitting

The electrochemical OER performance of as-prepared FCNP@CQDs nanotubes is tested using a three-electrode system in 1 M KOH seawater

solution. It is observed that the FCNP@CQDs present the lowest overpotential of 268 mV at 20 mA cm⁻² than these of FCNP electrode (without CQDs doping, 281 mV), FCN-LDHs@CQDs electrode (without phosphating process, 288 mV), FCN-LDHs electrode (nanorod structure, 311 mV), and MIL-88A@CQDs electrode (431 mV) (as shown in Fig. 5a). Comparing FCN-LDHs and FCN-LDH@CQDs electrodes as well as FCNP and FCNP@CQDs electrodes, the involved CQDs dramatically decrease the overpotential due to the increased conductivity and active centers [50]. The effect of phosphating process can also be observed by comparing FCNP@CQDs and FCN-LDHs@CQDs, as well as FCN-LDHs and FCNP. Especially for FCN-LDHs and FCNP, the overpotential decrease from 311 to 281 mV due to the increased conductivity. Combining the advantages of both CQDs and phosphating strategy, the FCNP@CQDs nanotube displays the lowest Tafel slope of 45.2 mV dec⁻¹ than that of the four contrast electrodes and commercial RuO₂, revealing a faster OER dynamic (Fig. 5b). The η₅₀ of 286 mV is 16, 28, 60 and 201 mV lower than FCNP, FCN-LDHs@CQDs, FCN-LDHs, and MIL-88A@CQDs electrode (Fig. 5c). Meanwhile, the samples with different cobalt-nickel ratio (Fig. S12), CQDs content (Fig. S13), phosphating temperatures (Fig. S14) and phosphating doses (Fig. S15) are also prepared and their OER performance are tested to obtain the best synthesis process.

In order to further understand the reaction kinetics of as-prepared samples, we conduct an electrochemical impedance test (Fig. 5d). The impedance is dramatically decreased from 16.1 (FCN-LDHs) to 6.8 Ω (FCNP) and 12 (FCN-LDHs@CQDs) to 6.1 Ω (FCNP@CQDs) by the phosphating process. the involved CQDs can also improving the conductivity of products from FCN-LDHs (16.1 Ω) to FCN-LDHs@CQDs (12 Ω) and FCNP (6.8 Ω) to FCNP@CQDs (6.1 Ω). Therefore, the FCNP@CQDs nanotube displays the smallest Rct value of 6.1 Ω than the other four samples, which means FCNP@CQDs present the best charge transfer rate for enhanced electrochemical performance. Furthermore, according to the cyclic voltammetry (CV) curve of the non-Faraday potential area (Fig. S16), the electrochemically active specific surface areas (ECSA) of the catalysts are estimated by the electric double layer

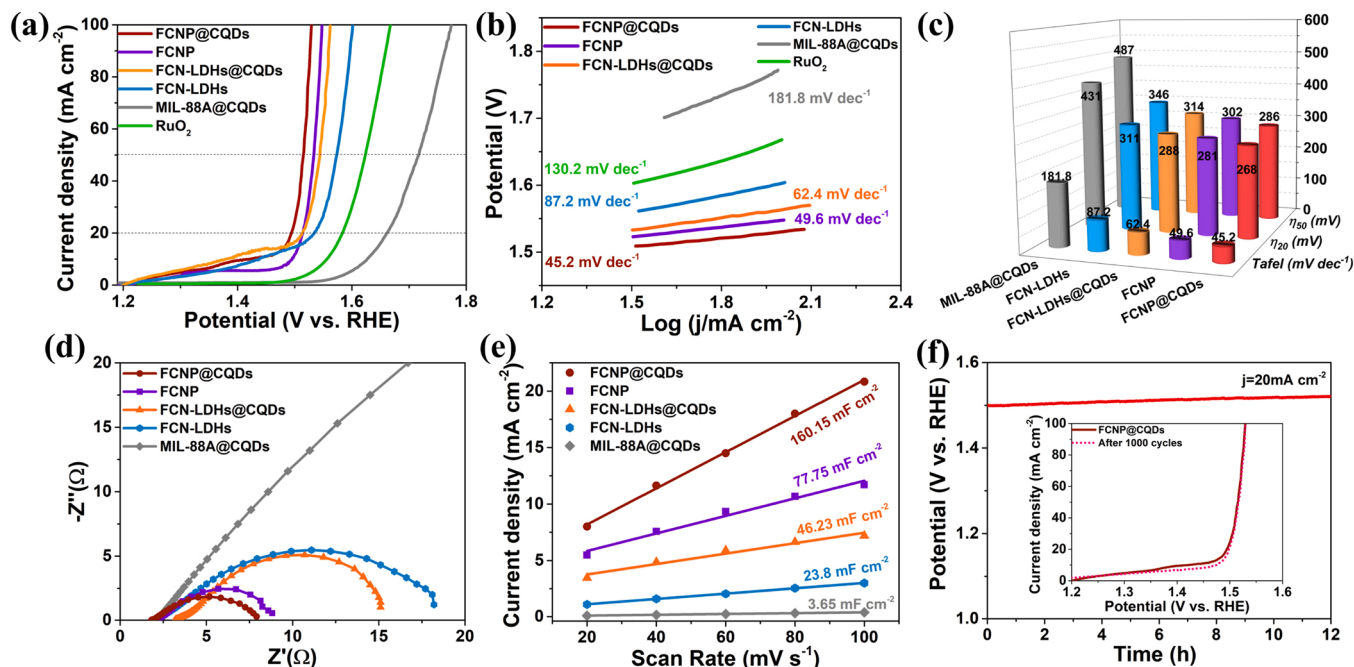


Fig. 5. (a) OER polarization curves, (b) Tafel slope, (c) Histograms reflecting η_{20} , η_{50} , and Tafel slope values, (d) Nyquist plots at 0.290 V, (e) C_{dl} curves of the OER, of FCNP@CQDs, FCNP, FCN-LDHs@CQDs, FCN-LDHs, and MIL-88A@CQDs. (f) CP curves of FCNP@CQDs at 20 mA galvanostatic current (inset compares the LSV curves of FCNP@CQDs before and after 1000 CV cycles).

capacitance (C_{dl}). The function graph of scanning speed and current density is shown in Fig. 5e. A high C_{dl} value of 160.15 mF cm⁻² is achieved for FCNP@CQDs nanotubes, which is larger than the slope of other samples (FCNP nanorods are 77.75 mF cm⁻², FCN-LDHs@CQDs nanotubes are 46.23 mF cm⁻², FCN-LDHs nanorods is 23.8 mF cm⁻², MIL-88A@CQDs is 3.65 mF cm⁻²). The result indicates that the involved CQDs can double the area of ECSA of FCNP. As a result, the FCNP@CQDs nanotube possesses the largest ECSA value, which may be the reason for the excellent OER performance of the FCNP@CQDs nanotube. Meanwhile, the stability of the FCNP@CQDs nanotube is also performed by

chronopotentiometry (CP). The potential (Fig. 5f) could be maintained at 20 mA cm⁻² during 12 h electrolysis, indicating remarkable stability. Furthermore, the long-time LSV (Linear sweep voltammetry) curve is also tested (Fig. 5f). After 1000 CV cycles, the LSV curve can overlap with the initial curves perfectly, which further confirms the outstanding stability of FCNP@CQDs nanotube under the alkaline OER process.

The HER performances of the samples are also tested in 1 M KOH seawater solution, and the LSV curves for the various electrodes are given in Fig. 6a. It is observed that the FCNP@CQDs possess the best HER performance with the overpotential η_{20} and η_{50} of 150 and 183 mV

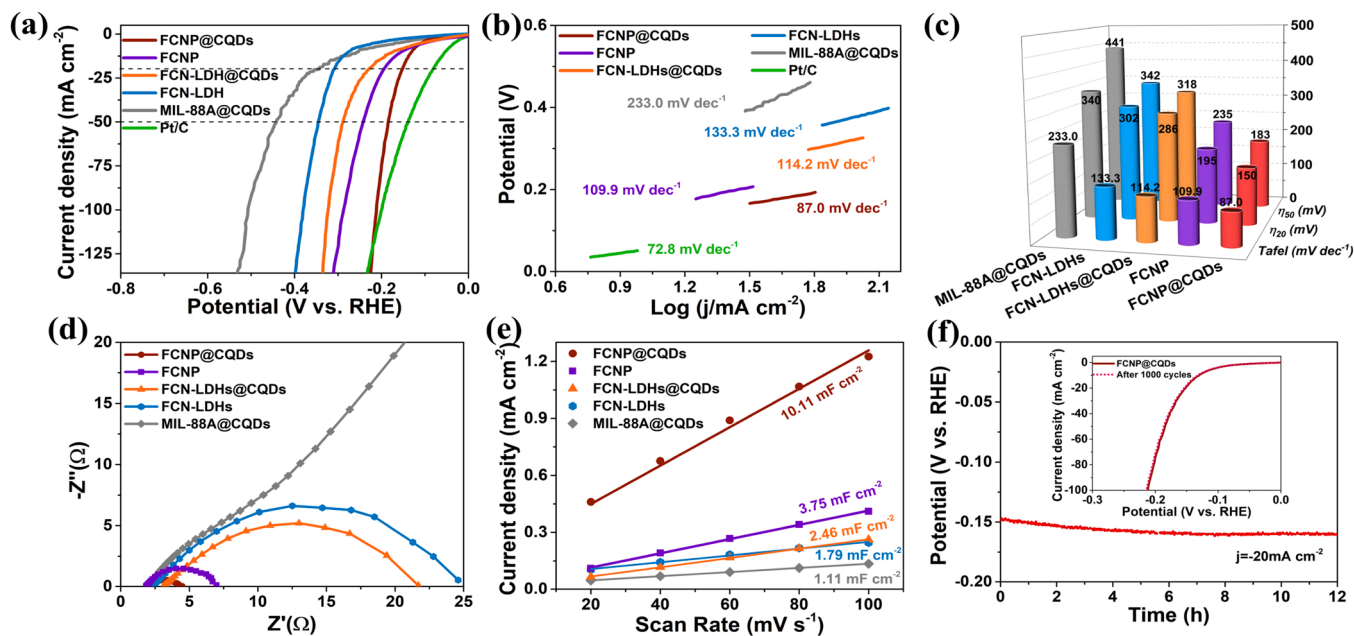


Fig. 6. (a) HER polarization curves of FCNP@CQDs, FCNP, FCN-LDHs@CQDs, FCN-LDHs, and MIL-88A@CQDs. (b) Tafel slope of different samples. (c) histograms reflecting η_{20} , η_{50} , and Tafel slope values of the as-formed products. (d) Nyquist plots at -0.150 V. (e) The C_{dl} curves of the HER. (f) CP curves of FCNP@CQDs at -20 mA galvanostatic current (inset compares the LSV curves of FCNP@CQDs before and after 1000 CV cycles).

than that of FCNP nanorods (195 mV, 223 mV), FCN-LDHs@CQDs nanotubes (286 mV, 318 mV), FCN-LDHs nanorods (302 mV, 342 mV), and MIL-88A@CQDs (340 mV, 441 mV), respectively (Fig. 6c). The polarization curves of FCNP@CQDs and Pt/C can overlap after the current densities up to 120 mA cm^{-2} , which indicates that the HER performance of FCNP@CQDs nanotubes is superior to that of Pt/C at high current density. The Tafel slope in the HER process is calculated (Fig. 6b), and the lower slope of the FCNP@CQDs nanotube indicates fast reaction kinetics of HER reaction. The electrochemical impedance spectroscopy shows that FCNP@CQDs, FCNP, FCN-LDHs@CQDs, and FCN-LDHs possess the charge transfer resistance of 2.38, 5.13, 18.61, and 22.4Ω (Fig. 6d), which further confirm the promotion effect of CQDs doping and phosphating process on electron transfer. The results of hydrophilic experiments show that FCNP@CQDs deliver a contact angle of almost 0° , which presents excellent hydrophilic performance than FCNP with a contact angle of 35.4° (Fig. S17). Meanwhile, the ECSA of each catalyst is also evaluated by the C_{dl} value, according to the CV of each catalyst at different sweep speeds (Fig. S18), and the plot of Δj with the sweep speed at 0.095 V (vs. RHE) (Fig. 6e). It is observed that the largest C_{dl} value of 10.1 mF cm^{-2} than the other four electrodes, indicating that the combination of open and hollow nanotube structure and the involved CQDs can provide the largest active center for HER process. In addition, the stability of FCNP@CQDs nanotubes is evaluated by the polarization curve after 1000 cycles and the CP curve at 20 mA cm^{-2} (Fig. 6f). After 12 h of CP testing, the HER performance of FCNP@CQDs nanotubes is well maintained. The LSV curve after 1000 CV cycles can completely coincide with the original curve, which shows that the FCNP@CQDs nanotube has excellent durability.

Due to the outstanding HER and OER performance of FCNP@CQDs nanotubes, it is possible to construct an overall seawater electrolysis system with FCNP@CQDs as both cathode and anode. Fig. 7a shows that the FCNP@CQDs nanotubes need a voltage of 1.61 V to achieve 10 mA cm^{-2} , while FCN-LDHs@CQDs nanotubes require a larger voltage (1.7 V) to achieve the same current density. The LSV curves of FCNP@CQDs present a higher slope than that of FCN-LDHs@CQDs,

indicating a higher reaction kinetics. With the increasing current density from 10 to 50 mA cm^{-2} , the potential difference of FCNP@CQDs and FCN-LDHs@CQDs changes from 90 to 194 mV, indicating that FCNP@CQDs have more favorable catalytic performance at higher currents. The catalytic performance of FCNP@CQDs is superior to that $\text{RuO}_2/\text{Pt/C}$ catalysts and reported bifunctional phosphide catalysts in Fig. 7a and b (details in Table S1). The stability FCNP@CQDs//FCNP@CQDs system is also evaluated by chronopotentiometry. Open hollow structures of FCNP@CQDs are well maintained during the HER and OER process, and the potential is only increased by 3% after 50 h of stability test, indicating that FCNP@CQDs nanotubes have excellent lifespan and structural stability (Fig. 7c and inset). During the electrolysis of seawater, large amounts of bubbles escape from the surface of cathode and anode, which can be collected and measured by the drainage method (Fig. 7e). Fig. 7d and f show the images of collected gas on the anode and cathode per 8 min with total 48 min. The ratio of hydrogen to oxygen produced is 1.92:1 (Fig. S19), which is close to 2:1 (theoretical value), indicating that no obvious chlorine is produced during the electrolysis process. What's more, the H_2 evolution rate is also evaluated, which is about 1 mmol h^{-1} during the period of 48 min

3.3. Theoretical study

To gain a deep insight of the active species and mechanism during the HER and OER process, the surface composition of the FCNP@CQDs catalyst after the stability test have been investigated. The XPS spectra of Fe, Co, and P elements are displayed in Fig. 8. The peaks of Fe-P species at 706.9 and 716.5 eV are well maintained after 50 h of cathodic reaction (HER). However, the characteristic peaks of Fe-P species completely disappeared after OER test (Fig. 8a). Similar phenomenon is also observed for the Co elements that the peaks of Co-P species also existed after HER but vanished after OER process. A new peak appeared in the Co 2p spectrum at 860.8 and 779.7 eV, respectively, corresponding to the existence of high valence states of Co^{3+} due to oxidation reaction (Fig. 8b) [51]. Similar oxidation phenomenon is also observed for the P

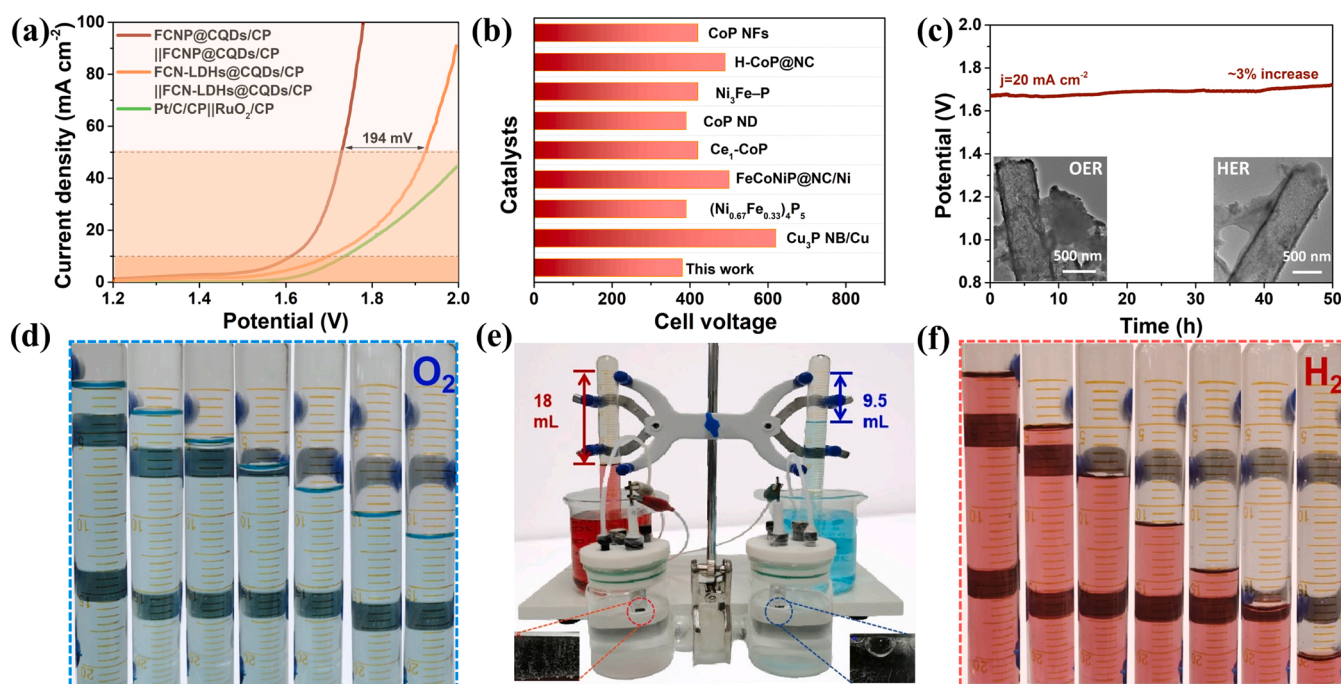


Fig. 7. (a) The polarization curves of FCNP@CQDs/CP||FCNP@CQDs/CP, FCN-LDHs@CQDs/CP||FCN-LDHs@CQDs/CP for total seawater splitting in 1 M KOH seawater electrolyzer. (b) Comparison of the overpotential (η_{10}) for overall water splitting between FCNP@CQDs/CP and other bifunctional electrocatalysts. (c) CP curve at 20 mA cm^{-2} of FCNP@CQDs/CP||FCNP@CQDs/CP. (d) Collected O_2 volume images generated every 8 min for 48 min, (e) H-type electrolytic cell device diagram, (f) Collected H_2 volume images generated every 8 min for 48 min of FCNP@CQDs/CP||FCNP@CQDs/CP.

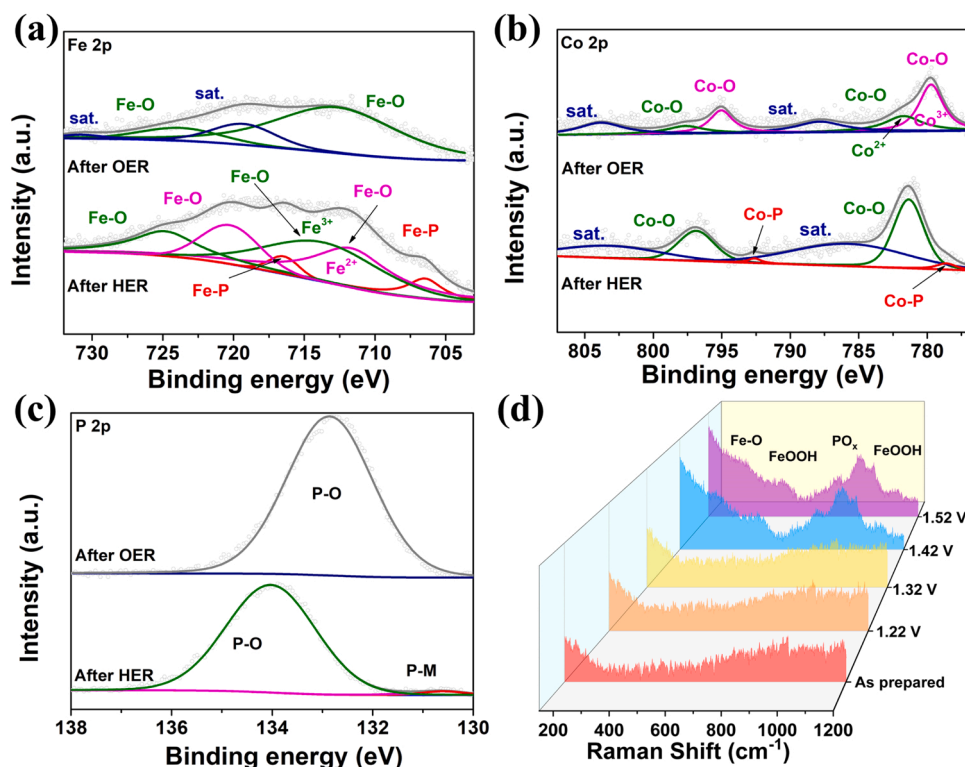


Fig. 8. XPS spectra of (a) Fe 2p, (b) Co 2p, (c) P 2p for FCNP@CQDs after 50 h OER and HER test. (d) *In-situ* Raman spectra of the FCNP@CQDs catalyst at various potentials for the OER process.

element and the peak of P-M disappeared to form high valence PO_x after the harsh OER reaction (Fig. 8c). Therefore, an inevitable surface phase transfer from Fe/Co/NiP to PO_x modified Fe/Co/Ni oxide/oxy(hydroxides), may occur at the anode. It is reported that the phosphates modified Fe/Co/Ni oxide/oxy(hydroxides) can stabilize the *OOH intermediate and repulse the surface adsorption of Cl^- , which may provide high OER kinetics and selectivity [52,53]. To further confirm the surface phase transfer process after OER process, the *in-situ* Raman tests of FCNP@CQDs catalysts during the OER reaction are performed at different potentials. As shown in Fig. 8d, a series of additional Raman bands appear within $100\text{--}1300\text{ cm}^{-1}$ when the voltage reaches 1.42 V. The peak at $\sim 335\text{ cm}^{-1}$ can be designated as Fe-O stretching vibration [49], and the peaks at ~ 530 and $\sim 1100\text{ cm}^{-1}$ belong to the Fe-O vibrations of FeOOH species [54,55], which further confirm the formation of Fe/Co/Ni oxide/oxy (hydroxides) species. Therefore, it can be assumed that the actual active species are FCNP@CQDs and Fe/Co/Ni-O/OH@CQDs for the cathode and anode, respectively.

4. Conclusions

In summary, a CQDs involved tri-metal phosphide (FCNP@CQDs) nanotube is successfully constructed by a selected etching and gas phosphating process via MIL-88A@CQDs as the precursor, which exhibits superior performances for HER and OER in alkaline seawater. During the etching process of MIL-88A@CQDs nanorod, both ends and the interior parts are corroded to form a hollow FCN-LDHs@CQDs, which is further phosphate by NaH_2PO_2 to obtain the target FCNP@CQDs nanotube. The doped Co and Ni elements achieves an effective adjustment of the electron structure of Fe centers, and the involved CQDs can provide more defects and voids for more accessible catalysis centers, which is benefit for the achievement of excellent catalysis performance. The OER test demonstrates that the FCNP@CQDs presents a low overpotential of 268 mV at 20 mA cm^{-2} , and a fast reaction kinetic with the Tafel slope of 45.2 mV dec^{-1} . The FCNP@CQDs

also displays remarkable HER activity with the overpotential η_{20} and η_{50} of 150 and 183 mV. Furthermore, FCNP@CQDs/CP||FCNP@CQDs/CP seawater electrolyzer is fabricated, which requires 1.61 V to reach 10 mA cm^{-2} in 1 M KOH seawater solution. An excellent stability is demonstrated in alkaline seawater with the potential only increased 3% after 50 h of stability test. The construction of the open hollow structure and embedded CQDs strategy may provide an effective way to design non-noble metal for stable and effective seawater electrocatalytic decomposition.

CRediT authorship contribution statement

Shujuan Lv: Sample preparation, Electrochemical testing, Data analysis and sorting, Writing manuscript. **Ying Deng:** Data analysis. **Qian Liu:** Data sorting. **Ziqi Fu:** Data analysis. **Xiaobin Liu:** Image analysis. **Minghui Wang:** Validation. **Zhenyu Xiao:** Revision of manuscript, Validation, Funding acquisition. **Bin Li:** Revision of manuscript, Validation. **Lei Wang:** Revision of manuscript, Validation, Funding acquisition.

Declaration of Competing Interest

The authors declare that they have no known competing financial interests or personal relationships that could have appeared to influence the work reported in this paper.

Data Availability

Data will be made available on request.

Acknowledgement

This work is financially supported from the National Natural Science Foundation of China (51772162 52072197 and 21971132), China

Postdoctoral Science Foundation (2020M682135), Postdoctoral Applied Research Project of Qingdao, Outstanding Youth Foundation of Shandong Province, China (ZR2019JQ14), Youth Innovation and Technology Foundation of Shandong Higher Education Institutions, China (2019KJC004), Major Scientific and Technological Innovation Project (2019JZZY020405), Major Basic Research Program of Natural Science Foundation of Shandong Province under Grant (ZR2020ZD09), and Taishan Scholar Young Talent Program (tsqn201909114).

Appendix A. Supporting information

Supplementary data associated with this article can be found in the online version at doi:10.1016/j.apcatb.2023.122403.

References

- [1] K.K. Gangu, S. Maddila, S.B. Mukkamala, S.B. Jonnalagadda, Characteristics of MOF, MWCNT and graphene containing materials for hydrogen storage: a review, *J. Energy Chem.* 30 (2019) 132–144, <https://doi.org/10.1016/j.jechem.2018.04.012>.
- [2] T. Li, T. Lu, X. Li, L. Xu, Y. Zhang, Z. Tian, J. Yang, H. Pang, Y. Tang, J. Xue, Atomically dispersed Mo sites anchored on multichannel carbon nanofibers toward superior electrocatalytic hydrogen evolution, *ACS Nano* 15 (2021) 20032–20041, <https://doi.org/10.1021/acsnano.1c07694>.
- [3] W. Zhou, M. Wu, G. Li, Rambutan-like CoP@Mo-Co-O hollow microspheres for efficient hydrogen evolution reaction in alkaline solution, *Chin. J. Catal.* 41 (2020) 691–697, [https://doi.org/10.1016/S1872-2067\(20\)63530-6](https://doi.org/10.1016/S1872-2067(20)63530-6).
- [4] C. Fu, X. Yan, L. Yang, S. Shen, L. Luo, G. Wei, J. Zhang, First-principles study of catalytic activity of W-doped cobalt phosphide toward the hydrogen evolution reaction, *Chin. J. Catal.* 41 (2020) 1698–1705, [https://doi.org/10.1016/S1872-2067\(20\)63622-1](https://doi.org/10.1016/S1872-2067(20)63622-1).
- [5] S.E. Hosseini, M.A. Wahid, Hydrogen production from renewable and sustainable energy resources: promising green energy carrier for clean development, *Renew. Sust. Energy Rev.* 57 (2016) 850–866, <https://doi.org/10.1016/j.rser.2015.12.112>.
- [6] F.M. Sapountzi, J.M. Gracia, C.J.K. Weststrate, H.O.A. Fredriksson, J.W. H. Niemantsverdriet, Electrocatalysts for the generation of hydrogen, oxygen and synthesis gas, *Prog. Energy Combust.* 58 (2017) 1–35, <https://doi.org/10.1016/j.pecc.2016.09.001>.
- [7] H. Jin, X. Liu, A. Vasileff, Y. Jiao, Y. Zhao, Y. Zheng, S. Qiao, Single-crystal nitrogen-rich two-dimensional Mo₅N₆ nanosheets for efficient and stable seawater splitting, *ACS Nano* 12 (2018) 12761–12769, <https://doi.org/10.1021/acsnano.8b07841>.
- [8] I. Staffell, D. Scamman, A. Velazquez Abad, P. Balcombe, P.E. Dodds, P. Ekins, N. Shah, K.R. Ward, The role of hydrogen and fuel cells in the global energy system, *Energy, Environ. Sci.* 12 (2019) 463–491, <https://doi.org/10.1039/C8EE01157E>.
- [9] L. Zhang, J. Wang, P. Liu, J. Liang, Y. Luo, G. Cui, B. Tang, Q. Liu, X. Yan, H. Hao, M. Liu, R. Gao, X. Sun, Ni(OH)₂ nanoparticles encapsulated in conductive nanowire array for high-performance alkaline seawater oxidation, *Nano Res.* 15 (2022) 6084–6090, <https://doi.org/10.1007/s12274-022-4391-6>.
- [10] S. Riyajuddin, M. Pahuja, P.K. Sachdeva, K. Azmi, S. Kumar, M. Afshan, F. Ali, J. Sultana, T. Maruyama, C. Bera, K. Ghosh, Super-hydrophilic leaflike Sn₄P₃ on the porous seamless graphene-carbon nanotube heterostructure as an efficient electrocatalyst for solar-driven overall water splitting, *ACS Nano* 16 (2022) 4861–4875, <https://doi.org/10.1021/acsnano.2c00466>.
- [11] F. Yu, H. Zhou, Y. Huang, J. Sun, F. Qin, J. Bao, W.A. Goddard, S. Chen, Z. Ren, High-performance bifunctional porous non-noble metal phosphide catalyst for overall water splitting, *Nat. Commun.* 9 (2018) 2551, <https://doi.org/10.1038/s41467-018-04746-z>.
- [12] Y. Li, Z. Dong, L. Jiao, Multifunctional transition metal-based phosphides in energy-related electrocatalysis, *Adv. Energy Mater.* 10 (2019), 1902104, <https://doi.org/10.1002/aenm.201902104>.
- [13] H. Xie, C. Lan, B. Chen, F. Wang, T. Liu, Noble-metal-free catalyst with enhanced hydrogen evolution reaction activity based on granulated Co-doped Ni-Mo phosphide nanorod arrays, *Nano Res.* 13 (2020) 3321–3329, <https://doi.org/10.1007/s12274-020-3010-7>.
- [14] L. Zhuang, J. Li, K. Wang, Z. Li, M. Zhu, Z. Xu, Structural buffer engineering on metal oxide for long-term stable seawater splitting, *Adv. Funct. Mater.* 32 (2022), 2201127, <https://doi.org/10.1002/adfm.202201127>.
- [15] X. Xiao, L. Yang, W. Sun, Y. Chen, H. Yu, K. Li, B. Jia, L. Zhang, T. Ma, Electrocatalytic water splitting: from harsh and mild conditions to natural seawater, *Small* 18 (2022), 2105830, <https://doi.org/10.1002/sml.202105830>.
- [16] L. Wu, L. Yu, F. Zhang, B. McElhenny, D. Luo, A. Karim, S. Chen, Z. Ren, Heterogeneous bimetallic phosphide Ni₂P-Fe₂P as an efficient bifunctional catalyst for water/seawater splitting, *Adv. Funct. Mater.* 31 (2021), 2006484, <https://doi.org/10.1002/adfm.202006484>.
- [17] D. Guo, X. Li, Y. Jiao, H. Yan, A. Wu, G. Yang, Y. Wang, C. Tian, H. Fu, A dual-active Co-CoO heterojunction coupled with Ti₃C₂-MXene for highly-performance overall water splitting, *Nano Res.* 15 (2022) 238–247, <https://doi.org/10.1007/s12274-021-3465-1>.
- [18] L. Wu, L. Yu, B. McElhenny, X. Xing, D. Luo, F. Zhang, J. Bao, S. Chen, Z. Ren, Rational design of core-shell-structured CoP@FeOOH for efficient seawater electrolysis, *Appl. Catal. B: Environ.* 294 (2021), 120256, <https://doi.org/10.1016/j.apcatb.2021.120256>.
- [19] S. Dresch, F. Dionigi, M. Klingenhof, P. Strasser, Direct electrolytic splitting of seawater: opportunities and challenges, *ACS Energy Lett.* 4 (2019) 933–942, <https://doi.org/10.1021/acsenenergylett.9b00220>.
- [20] F. Zhang, L. Yu, L. Wu, D. Luo, Z. Ren, Rational design of oxygen evolution reaction catalysts for seawater electrolysis, *Trends Chem.* 3 (2021) 485–498, <https://doi.org/10.1016/j.trechm.2021.03.003>.
- [21] P. Ding, H. Song, J. Chang, S. Lu, N-doped carbon dots coupled NiFe-LDH hybrids for robust electrocatalytic alkaline water and seawater oxidation, *Nano Res.* 15 (2022) 7063–7070, <https://doi.org/10.1007/s12274-022-4377-4>.
- [22] T. Ma, W. Xu, B. Li, X. Chen, J. Zhao, S. Wan, K. Jiang, S. Zhang, Z. Wang, Z. Tian, Z. Lu, L. Chen, The critical role of additive sulfate for stable alkaline seawater oxidation on Ni-based electrode, *Angew. Chem. Int. Ed.* 60 (2021) 22740, <https://doi.org/10.1002/anie.202110355>.
- [23] Y. Wang, B. Kong, D. Zhao, H. Wang, C. Selomulya, Strategies for developing transition metal phosphides as heterogeneous electrocatalysts for water splitting, *Nano Today* 15 (2017) 26–55, <https://doi.org/10.1016/j.nantod.2017.06.006>.
- [24] X. Sun, Ni foam-supported NiCoP nanosheets as bifunctional electrocatalysts for efficient overall water splitting, *Chin. J. Catal.* 40 (2019) 1405–1407, [https://doi.org/10.1016/S1872-2067\(19\)63443-1](https://doi.org/10.1016/S1872-2067(19)63443-1).
- [25] H. Zhang, A.W. Maijenburg, X. Li, S.L. Schweizer, R.B. Wehrspohn, Bifunctional heterostructured transition metal phosphides for efficient electrochemical water splitting, *Adv. Funct. Mater.* 30 (2020), 2003261, <https://doi.org/10.1002/adfm.202003261>.
- [26] Q. Kang, M. Li, J. Shi, Q. Lu, F. Gao, A universal strategy for carbon-supported transition metal phosphides as high-performance bifunctional electrocatalysts towards efficient overall water splitting, *ACS Appl. Mater. Inter.* 12 (2020) 19447–19456, <https://doi.org/10.1021/acsaami.0c00795>.
- [27] L. Wang, J. Fan, Y. Liu, M. Chen, Y. Lin, H. Bi, B. Liu, N. Shi, D. Xu, J. Bao, M. Han, Phase-modulation of iron/nickel phosphides nanocrystals “armored” with porous P-doped carbon and anchored on P-doped graphene nanohybrids for enhanced overall water splitting, *Adv. Funct. Mater.* 31 (2021), 2010912, <https://doi.org/10.1002/adfm.202010912>.
- [28] X.F. Lu, L. Yu, X. Lou, Highly crystalline Ni-doped FeP/carbon hollow nanorods as all-pH efficient and durable hydrogen evolving electrocatalysts, *Sci. Adv.* 5 (2019) v6009, <https://doi.org/10.1126/sciadv.aav6009>.
- [29] J. Joo, T. Kim, J. Lee, S.I. Choi, K. Lee, Morphology-controlled metal sulfides and phosphides for electrochemical water splitting, *Adv. Mater.* 31 (2019), 1806682, <https://doi.org/10.1002/adma.201806682>.
- [30] J. Zhang, M. Li, X. Liang, Z. Zhuang, Multishelled FeCo@FeCoP@C hollow spheres as highly efficient hydrogen evolution catalysts, *ACS Appl. Mater. Interfaces* 11 (2019) 1267–1273, <https://doi.org/10.1021/acsaami.8b17612>.
- [31] Q. Lv, J. Han, X. Tan, W. Wang, L. Cao, B. Dong, Featherlike NiCoP holey nanoarrays for efficient and stable seawater splitting, *ACS Appl. Energy Mater.* 2 (2019) 3910–3917, <https://doi.org/10.1021/acsaem.9b00599>.
- [32] M. Xiao, C. Zhang, P. Wang, W. Zeng, J. Zhu, Y. Li, W. Peng, Q. Liu, H. Xu, Y. Zhao, H. Li, L. Chen, J. Yu, S. Mu, Polymetallic phosphides evolved from MOF and LDH dual-precursors for robust oxygen evolution reaction in alkaline and seawater media, *Mater. Today Phys.* 24 (2022), 100684, <https://doi.org/10.1016/j.mphys.2022.100684>.
- [33] L. Wang, J. Wan, J. Wang, D. Wang, Small structures bring big things: performance control of hollow multishelled structures, *Small Struct.* 2 (2021), 2000041, <https://doi.org/10.1002/sstr.202000041>.
- [34] P. He, X. Yu, X.W.D. Lou, Carbon-incorporated nickel-cobalt mixed metal phosphide nanoboxes with enhanced electrocatalytic activity for oxygen evolution, *Angew. Chem. Int. Ed.* 56 (2017) 3897–3900, <https://doi.org/10.1002/anie.201612635>.
- [35] Y. Guo, J. Tang, Z. Wang, Y. Sugahara, Y. Yamauchi, Hollow porous heterometallic phosphide nanocubes for enhanced electrochemical water splitting, *Small* 14 (2018), 1802442, <https://doi.org/10.1002/sml.201802442>.
- [36] Q. He, H. Xie, Z.U. Rehman, C. Wang, P. Wan, H. Jiang, W. Chu, L. Song, Highly defective Fe-based oxyhydroxides from electrochemical reconstruction for efficient oxygen evolution catalysis, *ACS Energy Lett.* 3 (2018) 861–868, <https://doi.org/10.1021/acsenenergylett.8b00342>.
- [37] L. Ji, J. Wang, X. Teng, T.J. Meyer, Z. Chen, CoP nanoframes as bifunctional electrocatalysts for efficient overall water splitting, *ACS Catal.* 10 (2020) 412–419, <https://doi.org/10.1021/acscatal.9b03623>.
- [38] S. Wang, P. Yang, X. Sun, H. Xing, J. Hu, P. Chen, Z. Cui, W. Zhu, Z. Ma, Synthesis of 3D heterostructure Co-doped Fe₂P electrocatalyst for overall seawater electrolysis, *Appl. Catal. B: Environ.* 297 (2021), 120386, <https://doi.org/10.1016/j.apcatb.2021.120386>.
- [39] X. Yi, L. Song, S. Ouyang, N. Wang, H. Chen, J. Wang, J. Lv, J. Ye, Structural and component engineering of Co₂P&CoP@N-C nanoarrays for energy-efficient hydrogen production from water electrolysis, *ACS Appl. Mater. Inter.* 13 (2021) 56064–56072, <https://doi.org/10.1021/acsaami.1c15245>.
- [40] J. Jiao, W. Yang, Y. Pan, C. Zhang, S. Liu, C. Chen, D. Wang, Interface engineering of partially phosphidated Co@Co-P@NPCNTs for highly enhanced electrochemical overall water splitting, *Small* 16 (2020), 2002124, <https://doi.org/10.1002/sml.202002124>.
- [41] Y. Yan, J. Lin, J. Cao, S. Guo, X. Zheng, J. Feng, J. Qi, Activating and optimizing the activity of NiCoP nanosheets for electrocatalytic alkaline water splitting through the V doping effect enhanced by P vacancies, *J. Mater. Chem. A* 7 (2019) 24486–24492, <https://doi.org/10.1039/C9TA09283H>.

- [42] Y. Huang, L. Hu, R. Liu, Y. Hu, T. Xiong, W. Qiu, M.S.J.T. Balogun, A. Pan, Y. Tong, Nitrogen treatment generates tunable nanohybridization of Ni_5P_4 nanosheets with nickel hydr(oxy)oxides for efficient hydrogen production in alkaline, seawater and acidic media, *Appl. Catal. B: Environ.* 251 (2019) 181–194, <https://doi.org/10.1016/j.apcatb.2019.03.037>.
- [43] T. Wang, X. Cao, L. Jiao, $\text{Ni}_2\text{P}/\text{NiMoP}$ heterostructure as a bifunctional electrocatalyst for energy-saving hydrogen production, *eScience* 1 (2021) 69–74, <https://doi.org/10.1016/j.esci.2021.09.002>.
- [44] W. Chen, Z. Qin, B. McElhenny, F. Zhang, S. Chen, J. Bao, Z.M. Wang, H. Song, Z. Ren, The effect of carbon quantum dots on the electrocatalytic hydrogen evolution reaction of manganese-nickel phosphide nanosheets, *J. Mater. Chem. A* 7 (2019) 21488–21495, <https://doi.org/10.1039/C9TA06944E>.
- [45] J. Nai, Y. Lu, L. Yu, X. Wang, X.W.D. Lou, Formation of Ni-Fe mixed diselenide nanocages as a superior oxygen evolution electrocatalyst, *Adv. Mater.* 29 (2017), 1703870, <https://doi.org/10.1002/adma.201703870>.
- [46] Y. Yang, S. Wei, Y. Li, D. Guo, H. Liu, L. Liu, Effect of cobalt doping-regulated crystallinity in nickel-iron layered double hydroxide catalyzing oxygen evolution, *Appl. Catal. B: Environ.* 314 (2022), 121491, <https://doi.org/10.1016/j.apcatb.2022.121491>.
- [47] Z. Ran, C. Shu, Z. Hou, W. Zhang, Y. Yan, M. He, J. Long, Modulating electronic structure of honeycomb-like $\text{Ni}_2\text{P}/\text{Ni}_{12}\text{P}_5$ heterostructure with phosphorus vacancies for highly efficient lithium-oxygen batteries, *Chem. Eng. J.* 413 (2021), 127404, <https://doi.org/10.1016/j.cej.2020.127404>.
- [48] J. Lin, Y. Yan, T. Xu, J. Cao, X. Zheng, J. Feng, J. Qi, Rich P vacancies modulate $\text{Ni}_2\text{P}/\text{Cu}_3\text{P}$ interfaced nanosheets for electrocatalytic alkaline water splitting, *J. Colloid Interface Sci.* 564 (2020) 37–42, <https://doi.org/10.1016/j.jcis.2019.12.114>.
- [49] L. Yu, Q. Zhu, S. Song, B. McElhenny, D. Wang, C. Wu, Z. Qin, J. Bao, Y. Yu, S. Chen, Z. Ren, Non-noble metal-nitride based electrocatalysts for high-performance alkaline seawater electrolysis, *Nat. Commun.* 10 (2019) 5106, <https://doi.org/10.1038/s41467-019-13092-7>.
- [50] L. Tian, Z. Li, P. Wang, X. Zhai, X. Wang, T. Li, Carbon quantum dots for advanced electrocatalysis, *J. Energy Chem.* 55 (2021) 279–294, <https://doi.org/10.1016/j.jechem.2020.06.057>.
- [51] J. Liu, Y. Gao, X. Tang, K. Zhan, B. Zhao, B.Y. Xia, Y. Yan, Metal-organic framework-derived hierarchical ultrathin CoP nanosheets for overall water splitting, *J. Mater. Chem. A* 8 (2020) 19254–19261, <https://doi.org/10.1039/D0TA07616C>.
- [52] S. Li, Z. Li, R. Ma, C. Gao, L. Liu, L. Hu, J. Zhu, T. Sun, Y. Tang, D. Liu, J. Wang, A glass-ceramic with accelerated surface reconstruction toward the efficient oxygen evolution reaction, *Angew. Chem. Int. Ed.* 60 (2021) 3773–3780, <https://doi.org/10.1002/anie.202014210>.
- [53] J. Hausmann, P.W. Menezes, Effect of surface-adsorbed and intercalated (Oxy) anions on the oxygen evolution reaction, *Angew. Chem. Int. Ed.* 61 (2022), e202207279, <https://doi.org/10.1002/anie.202207279>.
- [54] M.W. Louie, A.T. Bell, An investigation of thin-film Ni-Fe oxide catalysts for the electrochemical evolution of oxygen, *J. Am. Chem. Soc.* 135 (2013) 12329–12337, <https://doi.org/10.1021/ja405351s>.
- [55] W.D. Chemelewski, H. Lee, J. Lin, A.J. Bard, C.B. Mullins, Amorphous FeOOH oxygen evolution reaction catalyst for photoelectrochemical water splitting, *J. Am. Chem. Soc.* 136 (2014) 2843–2850, <https://doi.org/10.1021/ja411835a>.